J Mater Sci
DOI 10.1007/s10853-012-6439-6

FIRST PRINCIPLES COMPUTATIONS

Properties of amorphous and crystalline titanium dioxide from first principles

Binay Prasai · Bin Cai · M. Kylee Underwood · James P. Lewis · D. A. Drabold

Received: 3 January 2012 / Accepted: 21 March 2012

Abstract We used first-principles methods to generate amorphous TiO_2 (a-TiO_2) models and our simulations lead to chemically ordered amorphous networks. We analyzed the structural, electronic, and optical properties of the resulting structures and compared with crystalline phases. We propose that two peaks found in the Ti–Ti pair correlation correspond to edge-sharing and corner-sharing Ti–Ti pairs. Resulting coordination numbers for Ti ($\sim$6) and O ($\sim$3) and the corresponding angle distributions suggest that local structural features of bulk crystalline TiO_2 are retained in a-TiO_2. The electronic density of states and the inverse participation ratio reveal that highly localized tail states at the valence band edge are due to the displacement of O atoms from the plane containing three neighboring Ti atoms; whereas, the tail states at the conduction band edge are localized on over-coordinated Ti atoms. The Γ-point electronic gap of $\sim$2.2 eV is comparable to calculated results for bulk crystalline TiO_2 despite the presence of topological disorder in the amorphous network. The calculated dielectric functions suggest that the amorphous phase of TiO_2 has isotropic optical properties in contrast to those of tetragonal rutile and anatase phases. The average static dielectric constant and the fundamental absorption edge for a-TiO_2 are comparable to those of the crystalline phases.

B. Prasai · B. Cai · D. A. Drabold (✉)
Department of Physics and Astronomy,
Ohio University, Athens, OH 45701, USA
e-mail: drabold@ohio.edu

M. K. Underwood · J. P. Lewis
Department of Physics, West Virginia University,
Morgantown, WV 26506, USA

Introduction

The discovery of titanium dioxide's ability to split water by photocatalysis under ultraviolet light by Fujishima and Honda [1] has led to enormous work on the material (see Ref. [2] for a recent review). The hope is that titanium dioxide (TiO_2), widely used as a pigment in white paint and in sunscreen, may prove to be an economical material for use in photovoltaic, photocatalytic, and sensing applications [2].

The majority of studies on titania are based upon three crystalline phases (anatase, rutile, and brookite), as well as in multiple forms (bulk, nanoparticle, thin film, etc.). However, titania is naturally obtained as powder consisting of a mixture of crystalline and amorphous phases. Various methods have been employed to enhance the crystalline quality of titania (e.g., Ref. [3]). However, recent research, including the results presented herein, has focused on understanding the structural and electronic properties of amorphous titania (a-TiO_2) with the hope that the desirable properties of TiO_2 can be found in this less processed, thus cheaper, form of the material [4–9]. For example, a-TiO_2 has been synthesized as a tinted or enhanced photocatalyst [10, 11], used to purify dye-polluted water [12], and applied to resistive random access memory applications [13]. As more synthesis techniques, like those of Battiston et al. [14] and Zhao et al. [15], are developed to create a-TiO_2 thin films, a-TiO_2 will be used in applications traditionally reserved for crystalline TiO_2 or other more expensive amorphous films. Through our research, we aim for a deeper understanding of the energetic and electronic properties of a-TiO_2 while confirming structural properties to aid in the development of these materials as a viable solution to current energy and environmental issues.

Published online: 03 April 2012

Methods

We used the Vienna ab initio simulation program (VASP), a density functional code employing a planewave basis [16–18] to generate 96- and 192-atom structures of a-TiO_2 and crystalline TiO_2 (rutile and anatase) structures. Vanderbilt ultra-soft pseudopotentials [19] were used with the generalized gradient approximation (GGA) of Perdew–Wang 91 [20] throughout the calculations. We performed all molecular-dynamics simulations with a 1.6 fs time step using periodic boundary conditions at constant volume for annealing, equilibrating, and cooling, as well as a zero pressure conjugate gradient (CG) for relaxation (a safe 450 eV energy cutoff was used for the relaxation). The details of these simulations to generate the amorphous and crystal structures are presented herein. A preliminary form of this study appeared in a proceedings paper [21].

Amorphous TiO_2

We created a 192-atom model (64 Ti atoms and 128 O atoms) with a mass density of 3.8 g/cm^3; a smaller 96-atom supercell was cut out of the 192-atom system. The final models were then prepared by using the method of melt quenching [22]. Using this approach, we annealed the 192-atom model, then we equilibrated at 2500 K for 8 ps, well above the melting point (2116 K). We cooled this liquid TiO_2 system to 2200 K (slightly above the melting point) over 4.8 ps, and then equilibrated for another 4.8 ps. After these initial annealing and cooling simulations, we further cooled the TiO_2 system to 1100 K at the rate of 75 K/ps. At this stage in the procedure, we were able to observe primary structural features of a-TiO_2. After we equilibrated the system for another 2 ps at 1100 K, we further cooled the model to 300 K at the rate of 200 K/ps. After equilibrating for another 3.4 ps at 300 K, we quenched the model to its final ground state, fully optimized, structure. Two 96-atom model systems were prepared, using the same method as for the 192-atom model system, using two different rates of cooling (90 and 75 K/ps) between 2200 and 1100 K. The densities of all amorphous models were calculated after zero-pressure relaxation, and presented in Table 1.

Crystalline TiO_2

We used $2 \times 2 \times 2$ supercells for both rutile TiO_2 (32 atoms) and anatase TiO_2 (96 atoms) structures using the lattice parameters as provided in Ref. [23]. Both of the supercells were relaxed at zero pressure with CG option of VASP under similar condition as in a-TiO_2. For rutile supercell, a $4 \times 4 \times 6$ Monkhorst–Pack grid [24] was used for Brillouin-zone sampling whereas a $4 \times 4 \times 2$ grid was used for anatase supercell. The calculated densities and lattice parameters are presented in the Tables 1 and 2, respectively.

Table 1 Densities and total energies of a-TiO_2 models compared to crystalline phases

Model	Density (g/cm^3) (this study)	Density (g/cm^3) (Expt. [23])	E_{tot}/atom (eV)
96-Atom model I	3.59		−8.75
96-Atom model II	3.56		−8.85
192-Atom model	3.73		−8.80
Rutile TiO_2	4.13	4.25	−8.93
Anatase TiO_2	3.77	3.79	−8.95

Results and discussion

Partial pair correlation functions (PPCFs)

We used PPCFs to examine the local bonding environment of atoms in a-TiO_2. For all models, the PPCF confirmed a chemically ordered system with no homopolar bonding (Fig. 1). The use of the "cook and quench" method to fabricate the models is unbiased and its prediction of a perfectly chemically ordered network is therefore significant. This system displays substantial order in the local environment of the atoms marked by sharp initial peaks for all models, but exhibits no long-range order. Of particular interest are the two distinct initial peaks found for all models in the Ti–Ti pair correlation function. These two peaks, also found in a Reverse Monte Carlo (RMC) model [4], are attributed to two different environments for Ti atoms. The first peak corresponds to edge-sharing Ti–Ti pairs, whereas the second peak corresponds to corner-sharing Ti–Ti pairs. Although there is little variation in first peak position among the three models, the Ti–Ti distance is larger than the value of 3.0 Å obtained in the RMC model [4]. By normalizing the PPCF for Ti–Ti, we were able to calculate the fraction of edge-sharing Ti–Ti pairs denoted by this first peak as 0.29, 0.30, and 0.38 for the 96-atom model I, 96-atom model II, and 192-atom model, respectively. For the second peak position, we observe a larger variation among the three models (3.48–3.59 Å). These two Ti–Ti peaks are not unique to a-TiO_2 i.e., similar results are observed in crystalline TiO_2 with two Ti–Ti peaks at positions of 2.99 and 3.60 Å in rutile structure compared to 3.07 and 3.83 Å in anatase structure. Similarly, the width of the initial peak in the O–O pair correlation function also suggests both edge-sharing and corner-sharing environments for neighboring oxygen atoms, however, not so prominent as in the case of Ti–Ti. Again,

Table 2 Calculated crystal TiO_2 properties as compared to experiment and other computational methods (Ref. [25] PBE; Ref. [26] PW)

	Rutile			Anatase		
	$a = b$ (Å)	c (Å)	u	$a = b$ (Å)	c (Å)	u
This study	4.64	2.99	0.305	3.83	9.62	0.208
GGA [25]	4.67	2.97	0.305	3.80	9.67	0.207
GGA [26]	4.63	2.98	0.305	–	–	–
HF [27]	–	–	–	3.76	9.85	0.202
Expt. [23]	4.594	2.958	0.305	3.785	9.514	0.207

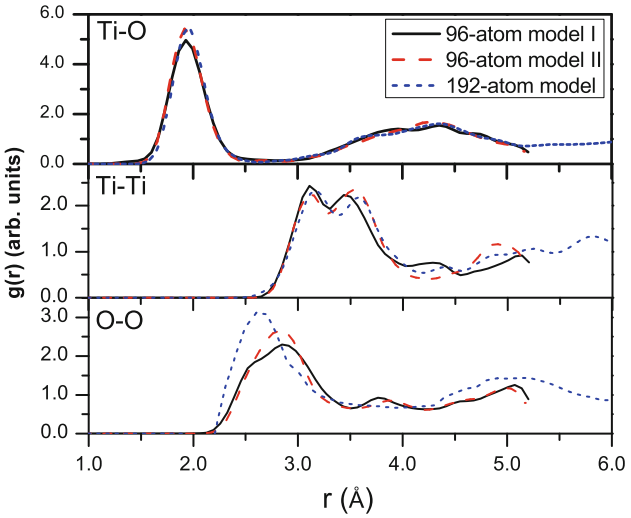

Fig. 1 (Color Online) PPCFs for Ti–O, Ti–Ti, and O–O coordination of the three a-TiO_2 models (96-atom model I, 96-atom model II, and 192-atom model, respectively) are plotted

the calculated average O–O first peak position (2.85, 2.83, and 2.74 Å in 96-atom models I and II, and 192-atom model, respectively) is slightly over-estimated in all three models compared to the experimental value of 2.67 Å [4]. Like Ti, O also has both edge-sharing and corner-sharing environments with O–O distances of 2.56 Å (2.49 Å) and 2.8 Å (2.82 Å), respectively, in rutile (anatase) structure. Conversely, the calculated first peak position in the Ti–O correlation of 1.92–1.94 Å is slightly less than the experimental Ti–O average bond distance of 1.96 Å [4]. In crystalline TiO_2, two types of Ti–O pairs are observed with bond lengths of 1.98 and 2.00 Å in the rutile structure, and 1.96 and 2.00 Å in the anatase structure. These numbers are, however, slightly over-estimated compared to those observed experimentally (1.946 and 1.984 Å in rutile and 1.937 and 1.964 Å in anatase [28]). More detailed information on measured nearest neighbor bond distances is presented in Table 3. While all models are consistent with experiment, we attribute variation among the models, both with each other and as compared to experiment, to limited statistics from a small collection of small models. From the PPCF data, we found the mean coordination numbers of Ti to be 5.47, 5.50, and 5.76, and the coordination numbers of O to be 2.73, 2.74, and 2.88 for the 96-atom model I, 96-atom model II, and the 192-atom model, respectively. These results are consistent with the RMC and experimental coordination numbers of Ti (5.6 ± 10%) and O (2.8 ± 10%) [4]. Complete coordination statistics are presented in Table 4. This reveals that the local structure of a-TiO_2 resembles that of crystalline TiO_2 where Ti atoms prefer to bond with six oxygen neighbors that form an octahedral structure, and O atoms prefer three titanium atoms as neighbors.

Bond angle distributions

We plot and analyze the Ti–O–Ti and O–Ti–O angle distributions of all three a-TiO_2 models to gain a better understanding of the simulated structures, plotted in Fig. 2. When compared to the angle distributions for the rutile and

Table 3 Mean nearest neighbor bond lengths in a-TiO_2 (in Å). Ti–Ti_1 and Ti–Ti_2 refer to first and second peak of Ti–Ti correlation function

	Ti–O	Ti–Ti_1	Ti–Ti_2	O–O
96-Atom model I	1.92	3.08	3.48	2.85
96-Atom model II	1.91	3.07	3.53	2.83
192-Atom model	1.94	3.13	3.59	2.74
RMC + Expt. [4]	1.96	3.00	3.55	2.67
Rutile (this study)	1.97, 2.00	2.99	3.60	2.56, 2.80
Rutile (Expt. [28])	1.95, 1.98	2.96	3.57	2.53, 2.78
Anatase (this study)	1.96, 2.00	3.07	3.83	2.49, 2.82
Anatase (Expt. [28])	1.94, 1.96	3.03	3.78	2.45, 2.80

Table 4 Coordination statistics for amorphous and crystalline TiO_2 (in %)

	Ti_4	Ti_5	Ti_6	Ti_7	Ti_8	O_2	O_3	O_4	O_5	N_{Ti}	N_O
96-Atom model I	6.3	46.9	40.6	6.2	–	34.4	57.8	7.8	–	5.47	2.73
96-Atom model II	3.1	53.1	37.5	3.1	3.1	29	67.7	3.2	–	5.50	2.74
192-Atom model	–	34.4	56.3	7.8	1.6	24.2	64.1	10.9	0.8	5.76	2.88
RMC + Expt. [4]	–	–	–	–	–	–	–	–	–	5.6	2.8
Crystalline TiO_2	–	–	–	–	–	–	–	–	–	6.0	3.0

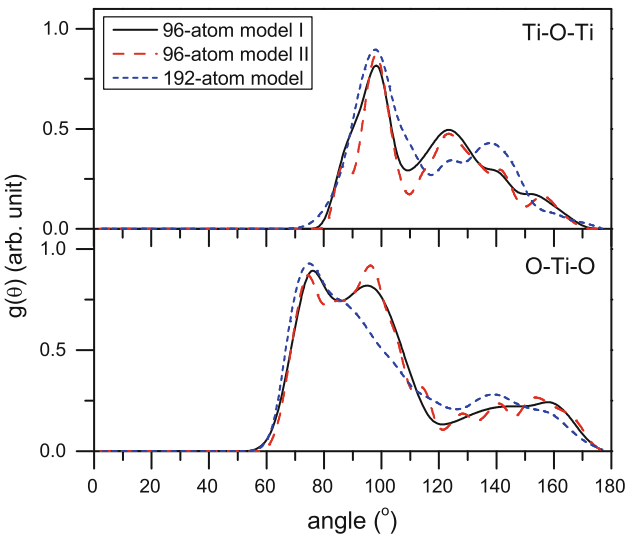

Fig. 2 (Color Online) Angle distributions are plotted for the three a-TiO_2 models (96-atom model I, 96-atom model II, and 192-atom model). For comparison, the peaks for the Ti–O–Ti angle in anatase are 101.9° and 156.2° and in rutile are 98.7° and 130.6°; the peaks for the O–Ti–O angle in anatase are 78.1°, 92.4°, 101.9°, and 156.2° and in rutile are 81.3°, 90°, 98.7°, and 180°

anatase TiO_2 bulk crystalline structures, we observed that, much of the local crystalline topology is preserved in a-TiO_2. For comparison, the peaks for the Ti–O–Ti angle in anatase are 101.9° and 156.2° and in rutile are 98.7° and 130.6°; the peaks for the O–Ti–O angle in anatase are 78.1°, 92.4°, 101.9°, and 156.2° and in rutile are 81.3°, 90°, 98.7°, and 180°. Similar results were reported in Ref. [29]. We observe interesting features which appear to be unique to the a-TiO_2 models. For instance, in the plotted Ti–O–Ti angle distribution, all of the a-TiO_2 models show a large peak positioned near 98°. We attribute this peak to Ti–Ti edge-sharing pairs described by the first peak in the Ti–Ti pair correlation function. The subsequent peaks are therefore attributed to Ti–Ti corner-sharing pairs. The variation among models of these other peaks is consistent with the variation between models in the position of the second peak in the Ti–Ti pair correlation function. Similarly, we observe an initial peak in the O–Ti–O angle distribution near 75° for all three models and we attribute this peak to O–O edge-sharing pairs while subsequent peaks correspond to O–O corner-sharing pairs.

Electronic structure

We describe the main features of the electronic structure by analyzing the electronic density of states (EDOS), projected density of states (PDOS), and inverse participation ratio (IPR) of each individual site for each of the three a-TiO_2 models. Figure 3 shows the total EDOS of all three models with the Fermi level shifted to 0 eV. Excepting minor variations, the three EDOS are very similar. Furthermore, the total EDOS of a-TiO_2 is compared with that of the crystalline TiO_2 and presented in Fig. 4. The total EDOS of the a-TiO_2 is fairly close to those of crystalline TiO_2. For a deeper understanding we also analyzed the PDOS for all three a-TiO_2 models. We present the species PDOS and the orbital PDOS in Fig. 5. The lowest conduction band (CB) levels (near the Fermi level) are dominated by 3*d* states of Ti as in crystalline TiO_2 (both rutile and anatase). Also, similar to the crystalline phase, the valence band near the Fermi level has contributions from both 3*d* states of Ti and 2*p* states of O with oxygen 2*p* state dominating the tail region. Interestingly, we find that the Γ-point electronic gap of ∼2.22 eV is comparable to

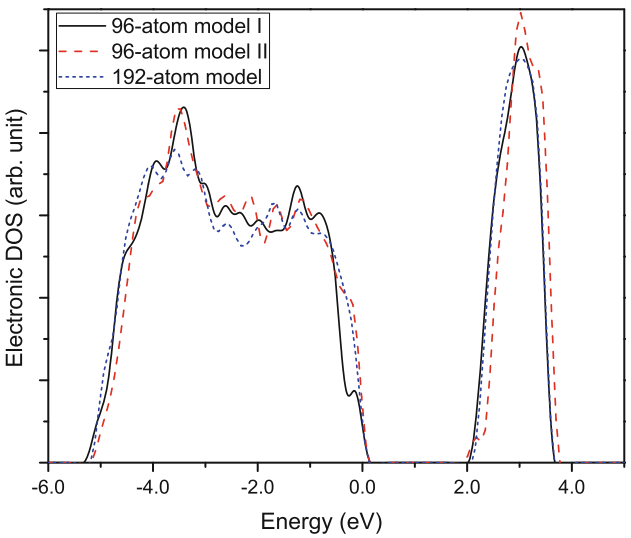

Fig. 3 (Color Online) EDOS (Γ point) for the three a-TiO_2 models (96-atom model I, 96-atom model II, and 192-atom model). Fermi level is at 0 eV

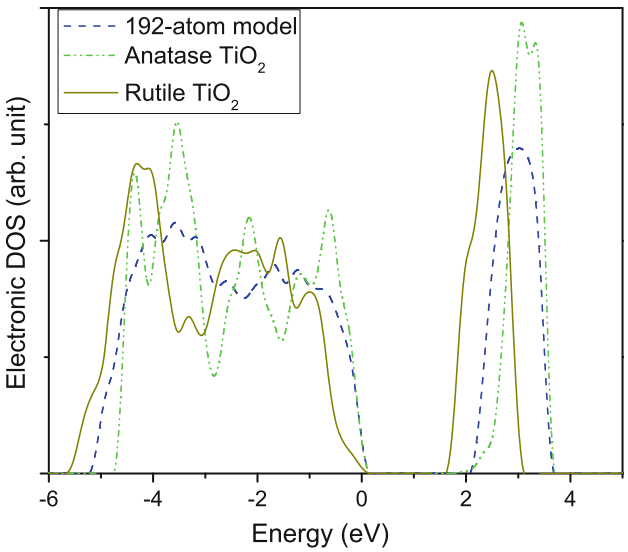

Fig. 4 (Color Online) EDOS for 192-atom a-TiO_2 model as compared with rutile and anatase TiO_2. Fermi level is at 0 eV

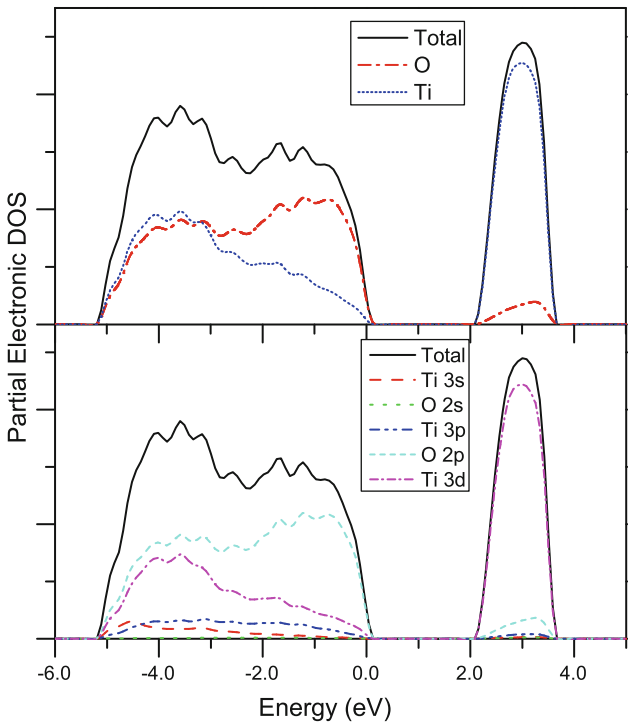

Fig. 5 (Color Online) Partial EDOS (Γ point) for the 192-atom a-TiO_2 model. The other two 96-atom a-TiO_2 models as well as crystalline TiO_2 yield similar results (not shown for simplicity). Fermi level is at 0 eV

the calculated results for bulk crystalline TiO_2 (1.73 eV for rutile and 2.02 for anatase). Similar results, as presented in Table 5, are reported from other calculations [25–27, 30].

One of the major characteristics of an amorphous material is the localization of the tail states near the band gap in contrast to the completely delocalized tail states in a crystalline material. We used an IPR analysis to investigate the localization of the tail states near the band gap [34] in the a-TiO_2 models. Figure 6 illustrates the IPR for all three models. Except for the 96-atom model II, we observed that the valence tail states are highly localized. On the other hand, conduction tail states are relatively delocalized (except for in 96-atom model) somewhat reminiscent of a-GaN [35]. The valence tail states are localized on O-2*p* orbitals whereas conduction tail states are localized on Ti-3*d* orbitals. We analyzed the topology of the atoms associated with the tail states as indicated in the figure. All of the O atoms associated with the selected valence tail states (a–d) are threefold coordinated, whereas the Ti atoms associated with the conduction tail states (e–g) are more than sixfold coordinated. However, the O atom is displaced from the plane containing the neighboring Ti atoms, forming a pyramidal structure. This means that the over-coordinated Ti is the cause of the conduction tail states, whereas the positional disorder of O is the origin of the valence tail states.

Optical properties

We computed dielectric functions to characterize the optical properties for the crystalline (rutile and anatase) and the amorphous phases of TiO_2. Figure 7 presents the calculated real and imaginary parts of the dielectric functions for the three phases (two crystalline and one amorphous) of TiO_2 as a function of photon energy. Except for a few minor differences, both the real and the imaginary parts of the dielectric functions for anatase TiO_2 and a-TiO_2 closely resemble each other. The similarities of the optical properties between these phases can be attributed to the similar electronic structures. Moreover, the density of the a-TiO_2 is also much closer to that of anatase TiO_2. Rutile TiO_2 has significantly different features from other two phases in both the real and imaginary parts, owing to different electronic structures as compared to those phases. As the tetragonal cell of rutile and anatase is quite anisotropic, the optical properties are strongly dependent on the direction of the incoming polarized light, whereas, due to the isotropic nature of a-TiO_2 structure, the optical properties are independent on the direction of the incident light. To observe the optical anisotropy in different TiO_2 phases, we present the two components (perpendicular and parallel to *c* axis) of the imaginary parts of the dielectric functions in Fig. 8. We observed almost no change in the two components for a-TiO_2. The fundamental absorption edge, which results from the interband transition between the topmost valance band (VB) and the bottom of the CB, describes the optical band gap. We could not observe the sharp absorption edge which we attribute to the smaller size of the structures. We estimated the absorption edge by

Table 5 Comparison of electronic gaps (in eV) for different TiO_2 structures

	Rutile	Anatase	a-TiO_2
This study	1.73	2.02	2.22
GGAPBE [25]	1.86	2.25	–
PWGGA [26]	1.90	–	–
LDA [30]	1.78	2.04	–
Expt.	3.03 [31]	3.20 [32]	3.4 [33]

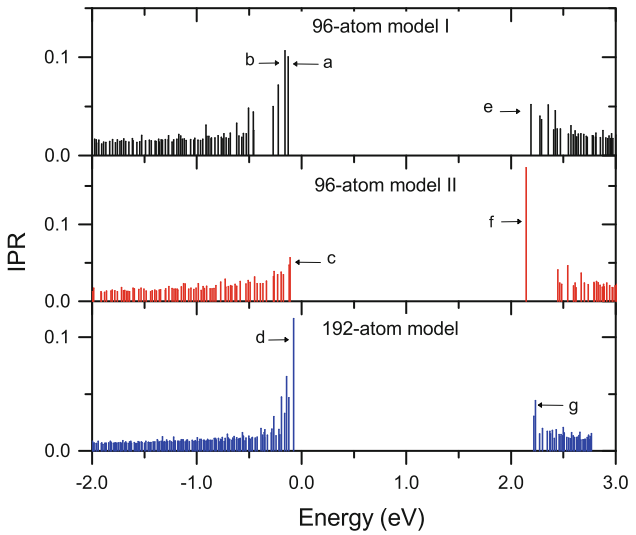

Fig. 6 (Color Online) IPRs are plotted for the three a-TiO_2 models (96-atom model I, 96-atom model II, and 192-atom model). Fermi level is shifted to 0 eV

extrapolating the perpendicular component of the imaginary part of the dielectric function, and found to be 1.8, 2.0, and 2.4 eV for rutile, anatase, and amorphous phases, respectively. These results for the crystalline TiO_2 phases are consistent with the results in Ref. [30]. The real part of the dielectric function as presented in Fig.7b is obtained from $\epsilon_2(\omega)$ by a Hilbert transform [36]. The static dielectric constant is obtained from the real part in the $\omega \rightarrow 0$ limit. The calculated values of the static dielectric constant were found to be 5.43, 4.3, and 4.1 (average for two models) for the rutile, anatase, and amorphous phases, respectively. In all respects the optical properties of the a-TiO_2 are quite similar to those of anatase phase TiO_2.

Conclusion

We created different a-TiO_2 models (two with 96 atoms and one with 192 atoms) by using the "melt-quench" method, and we were able to reproduce structural properties for a-TiO_2 as provided by experimental methods. Most

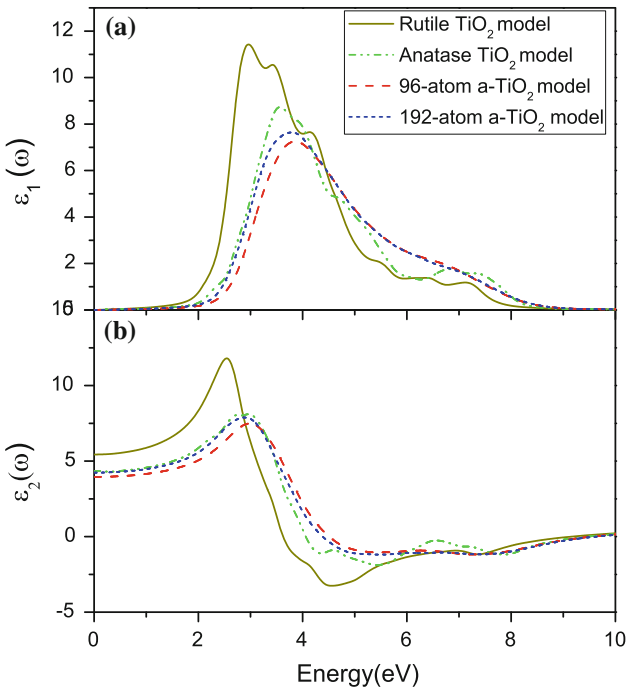

Fig. 7 (Color Online) Calculated imaginary parts (**a**) and real parts (**b**) of the dielectric function of TiO_2 for rutile, anatase, and amorphous structures

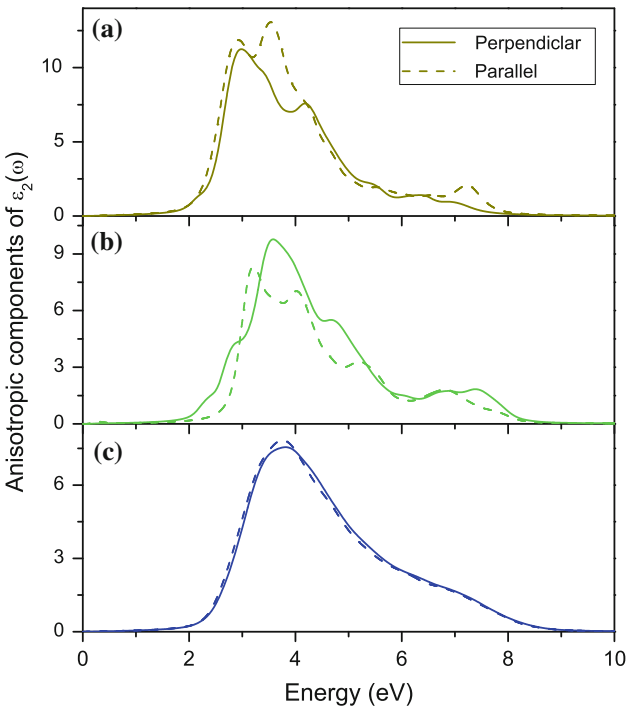

Fig. 8 (Color Online) Anisotropic components of imaginary part of the dielectric function; **a** rutile, **b** anatase, and **c** amorphous structures. Perpendicular components (to *c* axis) are *solid lines* and parallel components are *dashed lines*

of the Ti and O atoms tend to be sixfold and threefold coordinated, respectively, showing the similar local structure to crystalline form TiO_2 (both in the anatase and rutile structures). In addition, the electronic structures of a-TiO_2 is similar to the crystalline electronic structures in many respects, in fact much closer to the anatase TiO_2. The Γ-point band gaps of a-TiO_2 comparable to calculated results for bulk crystalline TiO_2 verifies the similarities. The IPR analysis showed that the tail states near the band edges are localized in a-TiO_2 in contrast to the crystalline TiO_2. The IPR analysis concluded that the valence tail states result from the positional disorder of O atoms, whereas, the conduction tail states result from over-coordinated Ti atoms. Furthermore, the optical properties of the a-TiO_2 resemble to those of anatase phase in many respects. The comparable structural, electronic, and optical properties between a-TiO_2 and crystalline TiO_2 opens the possibility of a-TiO_2 being used as an alternative to crystalline TiO_2 and hence reducing the cost of processing. As seen from the Weaire–Thorpe theorem [37] in amorphous Si, the electronic structure of a-TiO_2 is determined by the short range order of the network. As the local ordering is preserved within small distortions, the gross features of the electronic spectrum and dielectric functions are similar. All of this can be reformulated in terms of the decay of the density matrix in real space as discussed for example in Ref. [22].

Acknowledgements We thank NSF under DMR 0903225 for supporting this study. This study was also supported in part by an allocation of computing time from the Ohio Supercomputer Center.

References

1. Fujishima A, Honda K (1972) Nat Biotechnol 238:37
2. Chen X, Mao SS (2007) Chem Rev 107(7):2891
3. Yin H, Wada Y, Kitamura T, Kambe S, Murasawa S, Mori H, Sakata T, Yanagida S (2001) J Mater Chem 11(6):1694
4. Petkov V, Holzhüter G, Tröge U, Gerber Th, Himmel B (1998) J Non Cryst Solids 231(1–2):17
5. Zhang H, Banfield JF (2002) Chem Mater 14(10):4145
6. Hoang VV (2007) Phys Stat Solid B 244(4):1280
7. Hoang VV, Zung H, Trong NHB (2007) Eur Phys J D 44(3):515
8. Zhang HZ, Chen B, Banfield JF (2008) Phys Rev B 78(21):214106
9. Hoang VV (2008) Nanotechnology 19:105706
10. Zou JA, Gao JC, Xie FY (2010) J Alloy Compd 497(1–2):420
11. Randorn C, Irvine JTS, Robertson P (2008) Int J Photoenergy. Article ID 426872
12. Kanna M, Wongnawa S, Buddee S, Dilokkhunakul K, Pinpithak P (2010) J Sol Gel Sci Technol 53(2):162
13. Jeong HY, Lee JY, Choi SY (2010) Adv Funct Mater 20(22):3912
14. Battiston GA, Gerbasi R, Gregori A, Porchia M, Cattarin S, Rizzi GA (2000) Thin Solid Films 371(1–2):126
15. Zhao ZW, Tay BK, Yu GQ (2004) Appl Opt 43(6):1281
16. Kresse G, Furthmuller J (1996) Comput Mater Sci 6(1):15
17. Kresse G, Furthmuller J (1996) Phys Rev B 54(16):11169
18. Kresse G, Hafner J (1993) Phys Rev B 47(1):558
19. Vanderbilt D (1990) Phys Rev B 41(11):7892
20. Perdew JP, Burke K, Wang Y (1996) Phys Rev B 54(1):0163
21. Prasai B, Cai B, Underwood MK, Lewis JP, Drabold DA (2011) Materials Science and Technology Conference Proceedings, p 12
22. Drabold DA (2009) Eur Phys J B 68(1):1
23. Lide DR (ed) (1997) CRC handbook of chemistry and physics, 77th edn. CRC, Boca Raton
24. Monkhorst HJ, Pack JD (1976) Phys Rev B 13:5188
25. Shirley R, Kraft M (2010) Phys Rev B 81(7):075111
26. Islam MM, Bredow T, Gerson A (2007) Phys Rev B 76:045217
27. Fahmi A, Minot C, Silvi B, Causá M (1993) Phys Rev B 47:11717
28. Cromer DT, Herrington K (1955) J Am Chem Soc 77(18):4708
29. Howard CJ, Sabine TM, Dickson F (1992) Acta Cryst 47:462
30. Mo SD, Ching W (1995) Phys Rev B 51(19):13023
31. Amtout A, Leonelli R (1995) Phys Rev B 51(11):6842
32. Tang H, Berger H, Schmid PE, Lévy F, Burri G (1993) Solid State Commun 87:847
33. Valencia S, Marín JM, Restrepo G (2010) Open Mater Sci J 4:9
34. Atta-Fynn R, Biswas P, Ordejon P, Drabold DA (2004) Phys Rev B 69:085207
35. Cai B, Drabold DA (2011) Phys Rev B 84:075216
36. Cohen ML, Chelikowsky JR (1989) In: Cardona M (ed) Electronic structure and optical properties of semiconductors, 2nd edn. Springer, Berlin
37. Weaire D (1971) Phys Rev Lett 26:1541